

A Closer Look at Art Mediums: The MAMe Image Classification Dataset

Ferran Parés · Anna Arias-Duart · Dario Garcia-Gasulla · Gema Campo-Francis ·
Nina Viladrich · Eduard Ayguadé · Jesús Labarta

Received: date / Accepted: date

Abstract Art is an expression of human creativity, skill and technology. An exceptionally rich source of visual content. In the context of AI image processing systems, artworks represent one of the most challenging domains conceivable: Properly perceiving art requires attention to detail, a huge generalization capacity, and recognizing both simple and complex visual patterns. To challenge the AI community, this work introduces a novel image classification task focused on museum art mediums, the MAMe dataset. Data is gathered from three different museums, and aggregated by art experts into 29 classes of medium (*i.e.*, materials and techniques). For each class, MAMe provides a minimum of 850 images (700 for training) of high-resolution and variable shape. The combination of volume, resolution and shape allows MAMe to fill a void in current image classification challenges, empowering research in aspects so far overseen by the research community. After reviewing the

singularity of MAMe in the context of current image classification tasks, a thorough description of the task is provided, together with dataset statistics. Baseline experiments are conducted using well-known architectures, to highlight both the feasibility and complexity of the task proposed. Finally, these baselines are inspected using explainability methods and expert knowledge, to gain insight on the challenges that remain ahead.

Keywords Image Classification · High-resolution images · Variable-shaped images · Artwork Medium · Dataset

1 Introduction

Challenging problems is what drives AI research. What pushes the field and its applications forward. A prime example of that is the ImageNet dataset, together with the corresponding ILSVRC challenge [37]. The popularization of this competition revitalized the Neural Networks field, particularly in the context of image processing. The outstanding performance of deep neural networks models

Ferran Parés
Barcelona Supercomputing Center (BSC)
E-mail: ferran.pares@bsc.es

Anna Arias-Duart
Barcelona Supercomputing Center (BSC)
E-mail: anna.ariasduart@bsc.es

Dario Garcia-Gasulla
Barcelona Supercomputing Center (BSC)
E-mail: dario.garcia@bsc.es

Gema Campo-Francis
Conservaci-Restauraci Universitat de Barcelona (UB)

Nina Viladrich
Conservaci-Restauraci Universitat de Barcelona (UB)

Eduard Ayguadé
Barcelona Supercomputing Center (BSC)
Universitat Politcnica de Catalunya (UPC)

Jesús Labarta
Barcelona Supercomputing Center (BSC)
Universitat Politcnica de Catalunya (UPC)



Fig. 1: Subset of images from the official MAMe dataset. Notice the variation in shape among images.

in the demanding ILSVRC challenge caught the attention of AI researchers and practitioners around the world, who quickly acknowledged the potential behind the combination of deep nets and large sets of data. As a result, the popularity of the field exploded.

The ImageNet dataset provided an appealing challenge to lure AI researchers, who in turn were able to develop and test new ideas on it. Some of these ideas became powerful principles for the current deep learning (DL) field, such as Inception blocks [45], residual connections [20], dropout regularization [42], ReLU activations [32] and weight initializations [15, 18], among others. This amounts for a remarkable set of achievements in a very short time span, and speaks of the contribution of ImageNet to the AI field. That being said, the relevance of the ImageNet image classification challenge today has mostly vanished. The last edition of ILSVRC took place in 2017 [1], and the AI community considers it a solved problem with little margin for improvement (by 2019, 98.2% top-5 accuracy [51] was achieved, while human top-5 classification accuracy is thought to be between 88% and 95% [37]).

The ImageNet challenge is defined around two main types of instances: Man-made objects, and living things. These classes are characterized by large distinctive features which require little attention to detail for their recognition. State-of-the-art performance can be achieved on this kind of tasks after applying heavy deformation on the image (*i.e.*, uniform reshape) and losing most visual details (*e.g.*, down-sampling to 300x300) [51]. At the same time, samples of the same class have little intra-class variance, while being affected by large contextual changes (background, scale, perspective, illumination, *etc.*). To contribute in a direction which has not yet been properly addressed by the AI community, in this paper we present a visual challenge which is different in all these aspects. It is based on museum art mediums (MAMe), where attention to detail is essential, where there is huge intra-class variance, and where contextual information is not a factor.

The properties of ImageNet and ImageNet-like datasets have popularized the practice of interpolating images. This approach allows to reduce the memory requirements of models, avoiding high-resolution (HR) images, and removing the hindrances of variable-shaped (VS) inputs. The first CNN models tackling the ImageNet challenge interpolated images to a fixed size of 224x224 pixels [40, 45]. More recent solutions increased that size to 229x229 [46], 331x331 [54], 480x480 [21] or even 600x600 [17, 26] pixels, as scaling the image resolution is known to result in better performances on some cases [14, 47]. Even so, the nature of the ImageNet-like problems minimized these inconveniences, resulting in competitive performances even when using relatively small input sizes [51]. Given the prominence of ImageNet, this particularity biased research.

Indeed, beyond this ImageNet-like tasks, there are many current and future visual challenges where the proper exploitation of HR and VS images is fundamental.

Visual challenges in the medical domain are often based on the identification of small-scale visual patterns, requiring both attention to detail and an understanding of large structures. In domains like breast cancer detection, the benefit of exploiting the highest possible image resolution has already been highlighted [13, 29], motivating the use of HR images. Similarly, image recognition systems used for autonomous driving also benefits from using HR images, as this entails detection at further distances, which have enormous safety implications. Current solutions already use images that are larger than 0.25 MP [9, 49].

The motivation for research on VS images derives from the increasing popularity of crowd-sourced datasets, like Open Images [24]. These datasets combine data produced from multiple sources, which saves time and effort, and increases data volume. However this typically implies that images are taken using all sorts of recording devices, which may have different resolution and aspect ratios. The orientation of the device when taking the picture can also result in dramatic shape variations (*i.e.*, landscape or portrait). In this context, the popular input uniformization approach seems potentially harmful.

This work introduces an image classification dataset containing images of HR and VS, where attention to detail is of capital relevance. Its purpose is to promote and empower research in areas previously overseen by the AI community. In §2, a sample of popular datasets are analyzed, in the context of our work. In §3, the main contribution is presented, the MAMe dataset. This section includes details regarding dataset construction (sources, task definition) as well as relevant statistics. To provide a first measure of the complexity problem, §4 presents baselines on the MAMe dataset using two well known architectures (VGG and ResNet). To illustrate the relevance of the HR and VS nature of MAMe, baselines are tested on a downsampled version of the data (including deformation and huge amount of information loss), and on a version which avoids deformation and reduces information loss. In §5, we get a better insight on the baseline results and the MAMe dataset through experts assessment, few small extra analysis and some explainability results. Finally, we conclude this contribution in §6.

2 Related work

There are many visual challenge datasets in the current literature. There are however, very few containing images larger than 500x500 pixels, and with a significant variance in their aspect ratio. To illustrate that point we analyze a sample of popular datasets which satisfy three conditions we consider essential for attracting and generating high quality research:

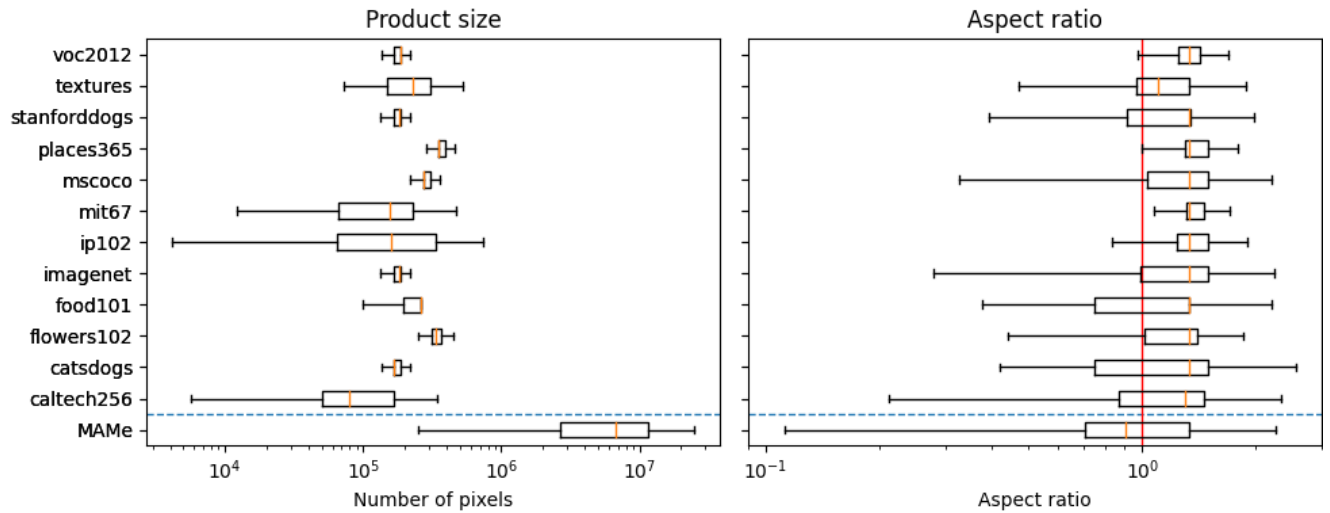


Fig. 2: Product size and aspect ratio distribution over several datasets, both on log scale. The dashed horizontal blue line separates a sample of current image classification datasets, and the proposed MAMe dataset. The vertical red line at aspect ratio 1.0 shows the border between portrait (left side) and landscape (right side) images.

- The dataset is publicly available.
- The dataset labels are reliable.
- The dataset has at least 100 instances per class.

The first requires data to be as public as possible, to reach the largest possible number of researchers. The second one excludes all datasets that contain labels not validated by humans or that have been crowd-labeled, as these may contain a significant amount of noise (and noise reduces the reliability of experimental results). The third enforces a minimum number of instances. We consider this a necessity for thorough research experimentation. We were nonetheless flexible in this regard, as some datasets of those analyzed contain some classes with less than 100 instances.

The sample analyzed contains the following 12 datasets: ImageNet 2012 [37], Food101 [8], IP102 [50], Places365 [53], Mit67 [35], Flower102 [33], CatsDogs [34], StanfordDogs [22], Textures [10], Caltech256 [16], Microsoft COCO [27] and Pascal VOC 2012 [11]. For each one we compute the product size (*i.e.*, width multiplied by height) and aspect ratio (*i.e.*, width divided by height) distributions. For the three datasets with more than 100,000 total samples (ImageNet 2012, Places365 and Microsoft COCO) we use a random sample of 100,000 images. Distributions for all 12 datasets can be seen in Figure 2.

In terms of number of pixels (left plot), current image classification datasets rarely contain images with more than 1 megapixel (MP). For reference purposes, none of the 12 datasets contain images bigger than 1,000 x 1,000 pixels, assuming unitary aspect ratio. This already indicates a significant bias in current research, and a mismatch with current technology, as popular image taking resolutions are well above that size. Obviously, there are datasets with images

larger than 1 MP, but these are typically either private, unreliability labeled [24], or have very few instances per class [12]. In this context, as shown at the bottom of Figure 2, the MAMe dataset stands out, containing a large volume of reliable labeled HR images. In fact, all images in the Q1-Q3 interval of the MAMe dataset are bigger than the largest image found on all analyzed datasets. The mean image size for the MAMe dataset is 6.6MP (*e.g.*, 2350x2350 in a squared image), one order of magnitude larger than all images contained in the analyzed datasets.

Regarding aspect ratio, the right plot of Figure 2 shows how the majority of images found in current datasets are landscape. All datasets have their median in the landscape side, only half of the datasets contain Q1 within the portrait side, and only 3 contain a significant amount of portrait images (Food101, CatsDogs and Caltech256). However, even these have their aspect ratio distribution clearly skewed towards landscape images (notice that the median is quite close to the third quartile on all three cases). In contrast, the proposed MAMe dataset has a balanced distribution, containing approximately the same number of portrait and landscape images. The aspect ratio distribution is also much wider than the other datasets, showing how the MAMe dataset contains infrequently wide and tall images.

3 The MAMe dataset

In this work we propose the Museum Artworks Medium dataset, abbreviated as the MAMe dataset. MAMe is an image classification dataset focused on the recognition of mediums in artworks and heritage held by museums (*e.g.*, *Oil on canvas*, *Bronze* or *Woodcut*). Medium is a broad tech-

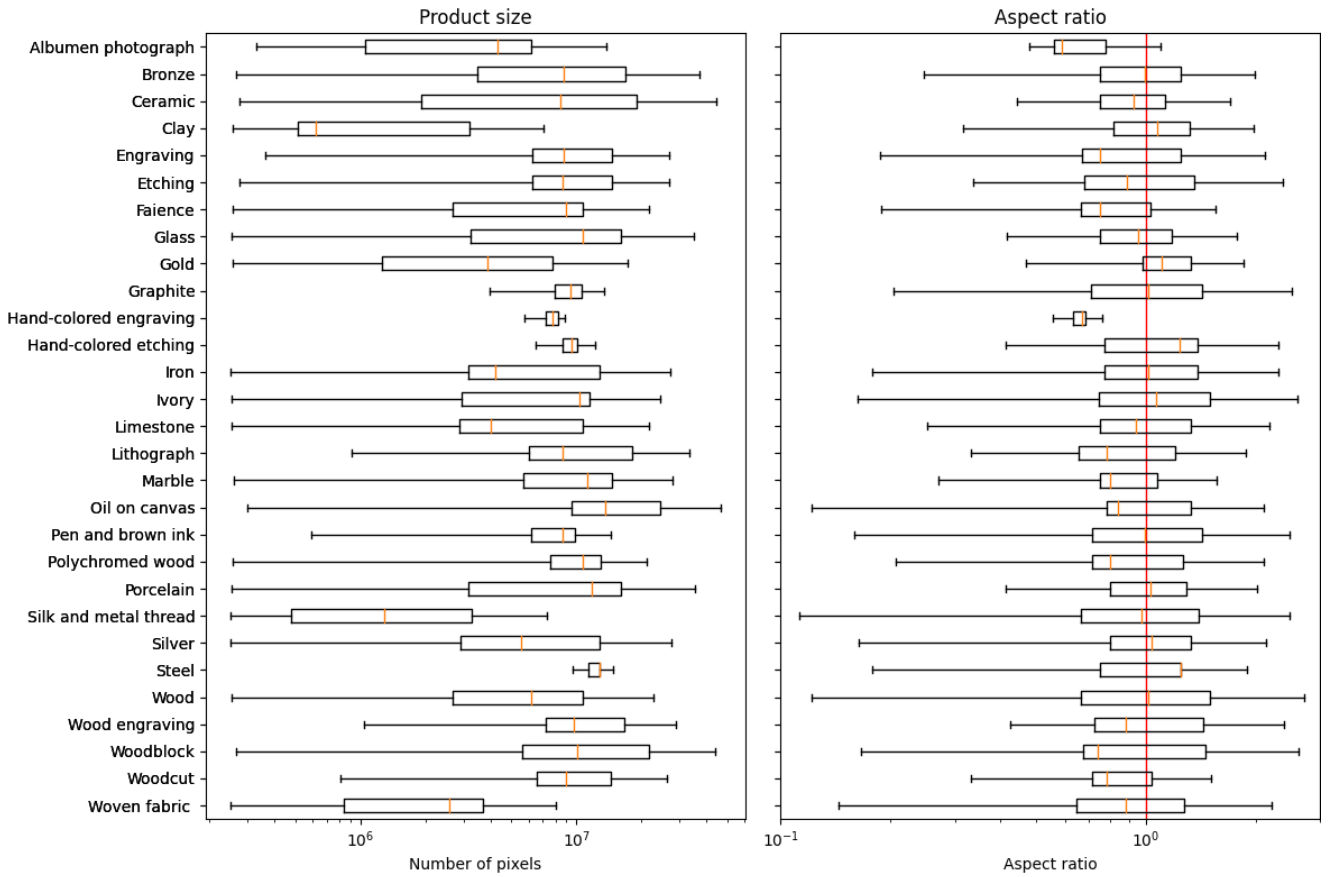


Fig. 3: Product size and aspect ratio distribution over all classes of the MAME dataset. Distributions are represented in box-plots, both of them on log scale. The vertical red line at aspect ratio 1.0 shows the border between portrait (left side) and landscape (right side) images.

nical term used to describe several aspects of artworks [30]. On one hand, it can be used to describe the main physical components used for the creation of an artwork, such as *Oil on canvas*. However, medium can also refer to the technique used to produce the artwork. *Engraving*, for example, is the printed result of engraving a metal plate. Both of these interpretations of medium are freely used by museums to organize their collections.

As detailed in §1, the classes considered in the MAME dataset comprise a wide variety of mediums according to both interpretations of the term. These can range from simple material aspects (e.g., *Bronze*, *Silver* or *Gold*) to complex, high-level techniques (e.g., *Faience*, *Woodblock* or *Woven fabric*). The variety of relevant features in MAME requires both attention to detail and to the overall image structure. Meanwhile, the essence of art causes widely different artworks to share the same label. The degree of intra-class variance of MAME is exemplified in Figure 4.

3.1 Data acquisition

In the past few years, museums around the world have been endorsing the policy of publicly releasing images of their heritage. Some of these museums release HR images under a CC0 license, allowing a free and unrestricted use of the data. We base our work on the data released by three museums. These were chosen because all three endorse the CC0 license, include a large number of images, provide accessible labels for them, and make it feasible to access their data in an automatized manner:

- The Metropolitan Museum of Art of New York (from now on the Met museum) [4].
- The Los Angeles County Museum of Art (from now on the Lacma museum) [3].
- The Cleveland Museum of Art (from now on the Cleveland museum) [2].

All three museums hold large artistic collections with a general scope, including artworks from all over the world, from very early cultures to recent ones. For accessing the data, the Cleveland museum publishes an API to automati-

Table 1: For each medium class within MAMe, distributions of instances among museums. The Met, Lacma and Cleveland museums are labeled as "Met", "Lac" and "Cle" respectively. Museum distributions are divided by data splits, into training, validation and test ("Train", "Val" and "Test" respectively). The last four columns show values aggregated for all data splits ("All"). The "Test" and "All" sections contain a 4th column indicating the total ("Total"). These values are not provided for "Train" and "Val" since these are constant (700 and 50 respectively).

Medium	Train			Val			Test				All			
	Met	Lac	Cle	Met	Lac	Cle	Met	Lac	Cle	Total	Met	Lac	Cle	Total
Albumen photograph	700	0	0	50	0	0	700	0	0	700	1450	0	0	1450
Bronze	234	233	233	16	17	17	233	233	234	700	483	483	484	1450
Ceramic	242	242	216	17	18	15	241	241	218	700	500	501	449	1450
Clay	695	5	0	49	1	0	310	2	1	313	1054	8	1	1063
Engraving	234	233	233	16	17	17	233	234	233	700	483	484	483	1450
Etching	234	233	233	16	17	17	233	234	233	700	483	484	483	1450
Faience	599	63	38	43	5	2	598	63	39	700	1240	131	79	1450
Glass	576	53	71	41	3	6	575	55	70	700	1192	111	147	1450
Gold	448	95	157	32	7	11	448	96	156	700	928	198	324	1450
Graphite	565	8	127	40	0	10	151	3	34	188	756	11	171	938
Hand-colored engraving	30	641	29	3	45	2	14	300	14	328	47	986	45	1078
Hand-colored etching	699	1	0	50	0	0	582	2	0	584	1331	3	0	1334
Iron	569	2	129	40	0	10	215	1	49	265	824	3	188	1015
Ivory	611	31	58	43	2	5	498	27	47	572	1152	60	110	1322
Limestone	593	56	51	42	5	3	591	56	53	700	1226	117	107	1450
Lithograph	277	147	276	19	11	20	276	148	276	700	572	306	572	1450
Marble	520	86	94	37	6	7	190	32	35	257	747	124	136	1007
Oil on canvas	265	171	264	18	12	20	264	172	264	700	547	355	548	1450
Pen and brown ink	665	12	23	47	1	2	271	6	9	286	983	19	34	1036
Polychromed wood	525	59	116	37	4	9	281	32	62	375	843	95	187	1125
Porcelain	447	56	197	31	4	15	446	57	197	700	924	117	409	1450
Silk and metal thread	680	0	20	48	0	2	92	1	2	95	820	1	24	845
Silver	452	81	167	32	5	13	450	83	167	700	934	169	347	1450
Steel	628	0	72	44	0	6	118	1	14	133	790	1	92	883
Wood	577	43	80	41	3	6	576	44	80	700	1194	90	166	1450
Wood engraving	410	15	275	29	1	20	211	9	141	361	650	25	436	1111
Woodblock	259	258	183	18	19	13	258	258	184	700	535	535	380	1450
Woodcut	417	51	232	30	3	17	416	52	232	700	863	106	481	1450
Woven fabric	658	3	39	46	0	4	656	5	39	700	1360	8	82	1450

cally download images. Lacma and Met on the other hand provide access to their images only through their webpages. This implies an image-by-image download process, for which we built museum-specific crawlers. By these means we downloaded approximately 232,000 images from the Met museum, 26,000 from the Lacma museum and 32,000 from the Cleveland museum. From this data, we define the MAMe dataset, composed by an expertly-curated subset of the data. The final selection includes 37,407 images belonging to 29 classes. The class selection process was made following several technical criteria, including balance between museums (to avoid potential bias), balance and volume of class instances (to facilitate research), and image resolution (to enable HR exploration). Grey scale images were discarded. Significantly, museum images have a natural tendency towards VS (*e.g.*, human sculptures tend to be tall, while paintings tend to be wide). Although we did not encourage its presence, this natural feature is shown in the dataset statistics (see right plot of Figure 3).

3.2 Label mapping

All three museums (Met, Lacma and Cleveland) reported the medium used to represent their artworks as metadata. Unfortunately, there is not a unique ontology behind, as each museum uses a different level of detail and interpretation of medium. Some mediums are subtypes of another mediums. Some mediums are reported under different names. And some mediums are combinations of other mediums. Experts from the art domain grouped the medium metadata into coherent classes, following their professional understanding of artistic coherency and visual discriminability. Classes which could not be discriminated visually by a human without technical aid (*e.g.*, a microscope) were discarded. The main expert criteria used to determine the classes are the following:

- Written coherency: Medium categories written in different forms referring to the same term are aggregated (*e.g.*, *Bronze* and *bronze*)

- Terminology coherency: Medium categories which are considered to be analogous are aggregated (e.g., *Ceramic* and *Pottery*).
- Taxonomic coherency: Object belonging to the same parent medium are sometimes aggregated (e.g., *Teracotta* and *Ceramic*). Where technical criteria allows, medium subtypes are left as a separate class (e.g., *Porcelain*, *Cotton* and *Linen* into *Woven fabric*).
- Visual coherency: Medium categories which cannot be visually differentiated at plain sight are aggregated (e.g., *Hard-paste porcelain* and *Soft-paste porcelain* into *Porcelain*, *Cotton* and *Linen* into *Woven fabric*).

After enforcing a minimum amount of 850 samples per medium (adding up train, val and test), the MAMe dataset contains 29 different classes. These are shown in the left column of Table 1. Notice we made an exception with the *Silk and metal thread* medium, which only contains 845 samples. A detailed description of the nature of each class is provided in Table 2. Visual details on how to discriminate some of these classes are discussed in §5.

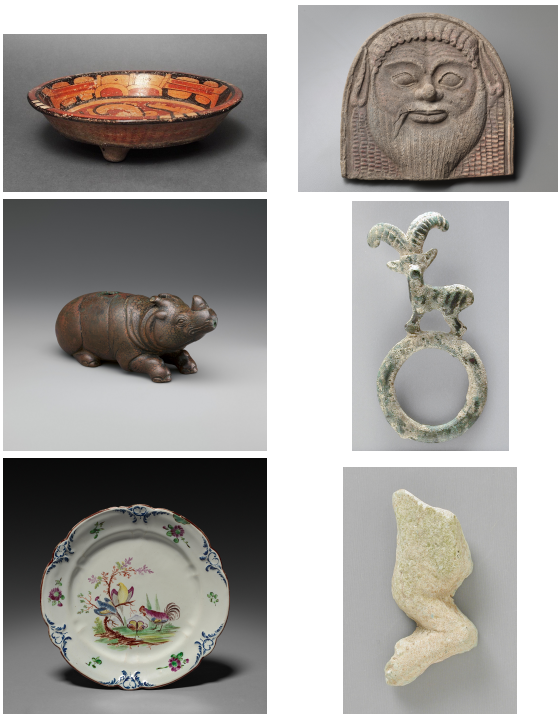


Fig. 4: Example of intra-class variance. Images in the same row belong to the same medium class, but share few visual features. The first row belongs to *Ceramic*, the second row to *Bronze* and the third row to *Faience*.

3.3 Dataset details

The MAMe dataset is publicly available¹. The site provides access to all the original images, and a CSV file with metadata for each of them. This metadata includes the following information:

- the **image filename**
- the **medium** of the artwork (i.e., the classification label)
- the **museum** from where the image was obtained
- the artwork **ID** given by the museum
- the **data split** of the instance (i.e., train, validation or test set)
- the **width** of the image
- the **height** of the image
- the **product size** of the image (i.e., width multiplied by height)
- the **aspect ratio** of the image (i.e., width divided by height)

The dataset contains 29 medium classes. Each class is composed by at least 850 images and, at most 1,450. Each class contains 700 images for training, 50 images for validation and a variable amount of images for the test set (i.e., the test set is unbalanced). The minimum amount of instances in the test set is 100 (except for *Silk and metal thread* with 95) and the maximum is 700. In total, the MAMe dataset is composed by 37,407 HR images. All images in the MAMe dataset have, at least, a resolution of 0.25MP, equivalent to a squared image of 500x500 pixels. The mean resolution is around 10.3MP, corresponding to an image of more than 3,200x3,200 pixels, and the greatest image has more than 370MP corresponding to an image of 32,683x11,412 pixels (check Figure 2). The 37,407 images are divided in subsets as follows: 20,300 images for training and 1,450 images for validation and 15,657 for test. Of those, 24,911 images originate from the Met museum, 5,531 images from the Lacma museum and 6,965 images from the Cleveland museum. An effort was made to keep the data coming from the different museums as balanced as possible, to minimize the possibility of potential biases generated by the nature of artworks and the image taking particularities of each museum. The exact distributions of images per museum, class and data split are shown in Table 1. To assess the internal balance of MAMe with regards to HR and VS features, Figure 3 shows the product size and aspect ratio distributions for each medium class. Besides a few classes with particularly narrow or skewed distributions, most of the categories include a wide variety of product sizes and aspect ratios.

¹ <https://hpaibsc.es/MAMe-dataset>

Table 2: Descriptions of the medium classes. Some descriptions are obtained from the museum sources [5].

Medium	Description
Albumen photograph	Photographic prints on paper support. Paper is coated with egg white and silver nitrate, and exposed to sunlight in contact with a glass negative.
Bronze	Objects mainly made of bronze (copper and tin alloy). Includes both polished and hammered bronze.
Ceramic	Includes pottery, stoneware, earthenware and terracotta. It may include glazed, slip-painted or painted textures.
Clay	Objects made of clay or mud. In most cases the object has not been baked, or it has at very low temperatures.
Engraving	Intaglio printmaking process in which lines are cut into a metal plate in order to hold the ink. The plate can be made of copper or zinc.
Etching	Intaglio printmaking process in which lines or areas are incised using acid into a metal plate in order to hold the ink. The plate can be made of iron, copper, or zinc.
Faience	May contain egyptian faience (sintered quartz with a vitreous coating) or tin-glazed pottery.
Glass	Objects mainly made of glass (eg blown, or pressed). Stained glass windows are excluded.
Gold	Objects mainly made of gold. Includes polished gold, hammered gold and other surface textures.
Graphite	Drawings or sketches made with graphite lead on paper.
Hand-colored engraving	Engraving prints hand-colored after the printmaking process. Prints are colored using either watercolor or wash techniques.
Hand-colored etching	Etching prints hand-colored after the printmaking process. Prints are colored using either watercolor or wash techniques.
Iron	Objects mainly made of iron. Includes polished iron, hammered iron and other surface textures.
Ivory	Objects made mainly of ivory (elephant or walrus tusks). Includes watercolor on ivory miniature portraits (medallions).
Limestone	Objects mainly made of limestone, a sedimentary rock mainly composed by calcium carbonate.
Lithograph	Planographic printmaking process in which a design is drawn onto a flat stone (or prepared metal plate, usually zinc or aluminum) and affixed by means of a chemical reaction. May contain lithographic offset prints and hand-colored monochrome lithographs.
Marble	Objects mainly made of marble, a metamorphic rock composed of calcite or dolomite.
Oil on canvas	Fabric stretched into frame (stretcher bar), with a preparation layer (or ground layer) painted with linseed oil and pigment.
Pen and brown ink	Drawings or sketches on paper, mainly made in brown ink (either with a dip pen, a fountain pen or a brush). Can be supplemented by other procedures such as wash (brown or black ink) or dry media. Some artworks may contain aged iron gall ink, or other similar brown inks such as bister or sepia ink.
Polychromed wood	Objects made of painted wood. Includes three-dimensional objects and painted surfaces, such as panel painting (oil on wood or tempera on wood).
Porcelain	A type of ceramic composed by quartz, feldspar and kaoli cooked at high temperatures. May contain soft-past porcelain.
Silk and metal thread	Woven fabric objects made of silk with metallic threads, typically forming an embroidery.
Silver	Objects mainly made of silver. Includes both polished and hammered silver.
Steel	Objects mainly made of steel (alloy of iron with carbon).
Wood	Non polychromed wood objects. Includes several wood types such as oak, boxwood or limewood.
Wood engraving	A type of woodcut printmaking process characteristic for using a block cut along the end-grain.
Woodblock	A type of woodcut printmaking process typically used by oriental cultures. This type of woodcut is carved along the wood grain and uses a different block for each color printed.
Woodcut	The oldest form of printmaking. Relief process in which knives and other tools are used to carve a design into the surface of a wooden block. The raised areas that remain after the block has been cut are inked and printed, while the recessed areas that are cut away do not retain ink, and will remain blank in the final print.
Woven fabric	Fabric objects woven with a loom. Includes linen, cotton, silk and others. Fabrics appear in several forms such as plain fabrics, embroideries or printed fabrics.

4 Baseline

This section introduces a baselines for the MAME dataset. Baselines illustrate how the task proposed is not trivial (*i.e.*, solved), coherently constructed (*i.e.*, solvable) and worth receiving the attention of researchers. To this end, we employ prototypical solutions that provide good results on other challenges, and report their performance on the MAME dataset. Baselines also offer a reference to future contributions, a performance to compare against and to measure progress. To provide a good reference to future contributions, we report learning curves, accuracy and other metrics.

All baseline models and the code needed to train them are publicly available ².

Through baselines we evaluate the relevance of image resolution and aspect ratio for the MAME dataset, a distinctive feature of the proposal. For each baseline architecture we experiment with two versions of the MAME dataset:

- The HR&VS-MAME version keeps the original aspect ratio of each image, avoiding deformation. It also maintains a HR standard, by scaling images until a minimum size of 500 pixels per axis (*e.g.*, a 2,000 x 1,000 pixels

² <https://github.com/HPAI-BSC/MAME-baselines>

image is transformed into 1,000 x 500 pixels and a 800 x 1,000 pixels image is transformed to 500 x 625 pixels).

- The LR&FS-MAME version has images of low resolution and fixed shape (LR&FS). All images are interpolated to a fixed size of 256 x 256 pixels. This implies deforming all images which are not originally squared.

The following subsection 4.1 describes the CNN designs used for the baselines. All data processing steps before feeding the CNNs are listed in 4.2. Afterwards, 4.3 provides the training configuration used for the baseline models. Finally, their performance on the MAME dataset is reported in 4.4.

4.1 Baseline Architectures

As baselines we use very well-known architectures: The VGG [40] and the ResNet [20]. Given the memory requirements of the MAME dataset and to facilitate training, we avoided the deepest versions of these designs. In our experiments we use the VGG11 (configuration A in [40]) and ResNet18 architectures.

Since the VGG is not originally input agnostic (*e.g.*, it cannot be trained with images of VS), we make one alteration to its design. We add an adaptive pooling layer [19] between the last convolutional layer and the first fully connected layer. The adaptive pooling layer is an improved and parameterized version of the global pooling that allows to specify the width and height of the output feature map so, instead of having an output of $1 \times 1 \times C$, where C stands for channels, we got $N \times N \times C$, where N is the size of the feature map we can decide. The N that we use for each architecture, is the one that produces the same feature map size than original architecture using the original input size: $N=7$ for VGG11 and $N=1$ for ResNet18.

During our experiments we had severe overfitting problems early in the training. This may be related with the high intra-class variance exhibited by the dataset, which drives learning towards highly specific and non-generalizable visual patterns. To mitigate that, the following regularization methods were used:

- Data augmentation: We apply several transformations to input images when training. First, we apply a random rotation in the range of $[-30, 30]$ degrees. Secondly, we apply a random crop of size $(0.875 \times \text{width}, 0.875 \times \text{height})$ pixels, corresponding to cropping from 256x256 to 224x224 pixels when using LR data. Finally, we randomly apply an horizontal flip with a 50% chance.
- Dropout: Only used on the VGG11 architecture, as stated in the original design [40]: Each neuron from fully-connected layers has a 50% chance of disabling its output.

Although the original ResNet18 architecture makes use of Batch Normalization [20], we deactivated it because it produced unstable training behaviours on the HR&VS experiment, hampering learning. For consistency purposes, Batch Normalization was disabled in both, LR&FS and HR&VS experiments using ResNet18.

4.2 Data Processing

In our experimentation, we consider two types of input processing. The first one, LR&FS, transforms the images as follows:

1. Resize image to 256x256 pixels.
2. Random rotation of the image from $[-30, 30]$ degrees.
3. Random crop of 224x224 pixels.
4. Random horizontal flip with 50% chance.
5. Normalize image values from range $[0, 255]$ to $[0, 1]$.
6. Standardize image values with $\mu = 0.5$ and $\sigma = 0.5$:

$$Output = \frac{Input - \mu}{\sigma}$$

When validating images through inference in the LR&FS experiments we do not perform the data augmentation. This implies avoiding steps 2 and 4, and to substitute step 3 by a Center crop of 224x224 pixels.

On the other hand, the input processing steps for HR&VS experiments are as follows:

1. Resize image maintaining its original aspect ratio forcing lowest dimension (either width or height) to be exactly 500 pixels.
2. Random rotation of the image from $[-30, 30]$ degrees.
3. Random crop of $(0.875 \times \text{width}, 0.875 \times \text{height})$ pixels. Width and height refer to current dimensions at this point of the processing.
4. Random horizontal flip with 50% chance.
5. Normalize image values from range $[0, 255]$ to $[0, 1]$.
6. Standardize image values with $\mu = 0.5$ and $\sigma = 0.5$:

$$Output = \frac{Input - \mu}{\sigma}$$

When validating the images of HR&VS experiments, we avoid data augmentation exactly as done in the LR&FS experiments. Again, we skip steps 2 and 4 while replacing step 3 by a center crop of $(0.875 \times \text{width}, 0.875 \times \text{height})$ pixels.

4.3 Training Parameters

All experiments used the AMSGrad optimizer [36], a variant of the original Adam optimizer [23]. Batch sizes and learning rates were optimized for both the LR&FS and HR&VS experiments separately, considering memory limitations,

Table 3: Mean per class accuracy for training, validation and test splits of the four baselines. The epoch used for the final model is specified in last column, which corresponds to the one with minimum validation loss. Best results in bold.

Experiment	MAMe Architect.	Accuracy			Model epoch
		Train	Val	Test	
LR&FS	VGG11	79.76%	70.21%	71.20%	27
	ResNet18	77.85%	65.66%	67.37%	43
HR&VS	VGG11	85.82%	74.55%	74.42%	41
	ResNet18	81.21%	70.48%	69.99%	47

training speed and learning convergence. For LR&FS experiments we used a batch size of 128 images and a learning rate of 0.00001 for VGG11, and 0.0001 for ResNet18. For HR&VS experiments, we used a batch size of a single image and a learning rate of 0.00001 for both architectures.

All experiments were conducted in a single computing node of the CTE-Power9 cluster at the Barcelona Supercomputing Center, with the following characteristics:

- 2 Sockets x IBM Power9 8335-GTH @ 2.4GHz (20 cores and 4 threads/core, total 160 threads).
- 4 x GPU NVIDIA V100 (Volta) with 16GB HBM2.

The computing time varies with the input data resolution and the architecture used. For the LR&FS experiments, the average time spent to process a training epoch with the VGG11 architecture was 399.1s, while for the ResNet18 architecture was 402.4s. For HR&VS experiments, the average time spent to process a training epoch was 712.0s using the VGG11 architecture and 696.9s using the ResNet18 architecture.

4.4 Experimental Results

In this section we evaluate a total of 4 baselines (two architectures, each trained on two versions of MAMe). The training and validation curves for all 4 cases are shown in Figure 5. Table 3 lists the accuracy obtained by each trained model. Additionally, we provide Table 4 showing the F1-scores for the best performing architecture (VGG11).

Results indicate a consistent gain in performance when using HR&VS dataset when compared to their interpolated versions. For VGG11, the improvement is of 3.22% in mean per class accuracy, while for the ResNet18 it is 2.62%. We are unable to assert to what degree is the gain caused by the increased information or by the deformation avoidance. Notice neither of these architectures has been designed or optimized for the use of high-resolution and variable-shaped inputs.

Even though the dataset is rather large in number of samples, the models converges in relatively few epochs. The VGG11 reaches minimum validation loss after 27 and

Table 4: F1-scores of VGG11 baseline models (both LR&FS and HR&VS). We include also the mean and difference (HR&VS minus LR&FS) of both F1-scores to illustrate the average performance of each class and the improvement when moving from LR&FS to HR&VS.

	LR&FS	HR&VS	Mean	Diff
Albumen photograph	0.9185	0.9485	0.9335	0.0300
Bronze	0.6185	0.7757	0.6971	0.1571
Ceramic	0.6671	0.6828	0.6750	0.0157
Clay	0.8019	0.8370	0.8194	0.0351
Engraving	0.6414	0.7900	0.7157	0.1485
Etching	0.5442	0.5114	0.5278	-0.0328
Faience	0.7971	0.8171	0.8071	0.0200
Glass	0.6628	0.7171	0.6900	0.0542
Gold	0.8542	0.8571	0.8557	0.0028
Graphite	0.8617	0.9148	0.8882	0.0531
Hand-colored engraving	0.9207	0.9756	0.9481	0.0548
Hand-colored etching	0.8818	0.8818	0.8818	0.0000
Iron	0.8037	0.8075	0.8056	0.0037
Ivory	0.5611	0.6083	0.5847	0.0472
Limestone	0.5957	0.5985	0.5971	0.0028
Lithograph	0.5471	0.7100	0.6285	0.1628
Marble	0.6420	0.7393	0.6906	0.0972
Oil on canvas	0.7228	0.7457	0.7342	0.0228
Pen and brown ink	0.8566	0.8181	0.8374	-0.0384
Polychromed wood	0.4826	0.4346	0.4586	-0.0480
Porcelain	0.8185	0.8714	0.8450	0.0528
Silk and metal thread	0.4526	0.6210	0.5368	0.1684
Silver	0.7400	0.7614	0.7507	0.0214
Steel	0.8345	0.8496	0.8421	0.0150
Wood	0.6371	0.6414	0.6392	0.0042
Wood engraving	0.8005	0.7091	0.7548	-0.0914
Woodblock	0.6685	0.7957	0.7321	0.1271
Woodcut	0.7328	0.7642	0.7485	0.0314
Woven fabric	0.4242	0.3971	0.4107	-0.0271

41 epochs for LR&FS and HR&VS experiments, while the ResNet does the same after 43 and 47 epochs, respectively.

Apart from reaching a better performance, HR&VS experiments seems to also reduce the gap between the training and validation curves. This is clearly seen on the ResNet18 experiments but almost non-existent on the VGG11 experiments. These results suggest that using images of high-resolution with their original aspect ratios may have desirable regularization effects. However, further experimentation is needed to properly validate this conclusion.

The F1-scores Table 4 indicates the improvements on performance at class granularity level. In general, all classes show an improvement on performance when passing from LR&FS to HR&VS, except for few ones (5 out of 29). For analysis purposes, this table also shows the mean accuracy per class, providing a first insight on which MAMe dataset classes harder to learn. In section 5.2 and 5.3, we discuss further about these differences, complementing them with the perspective of art experts.

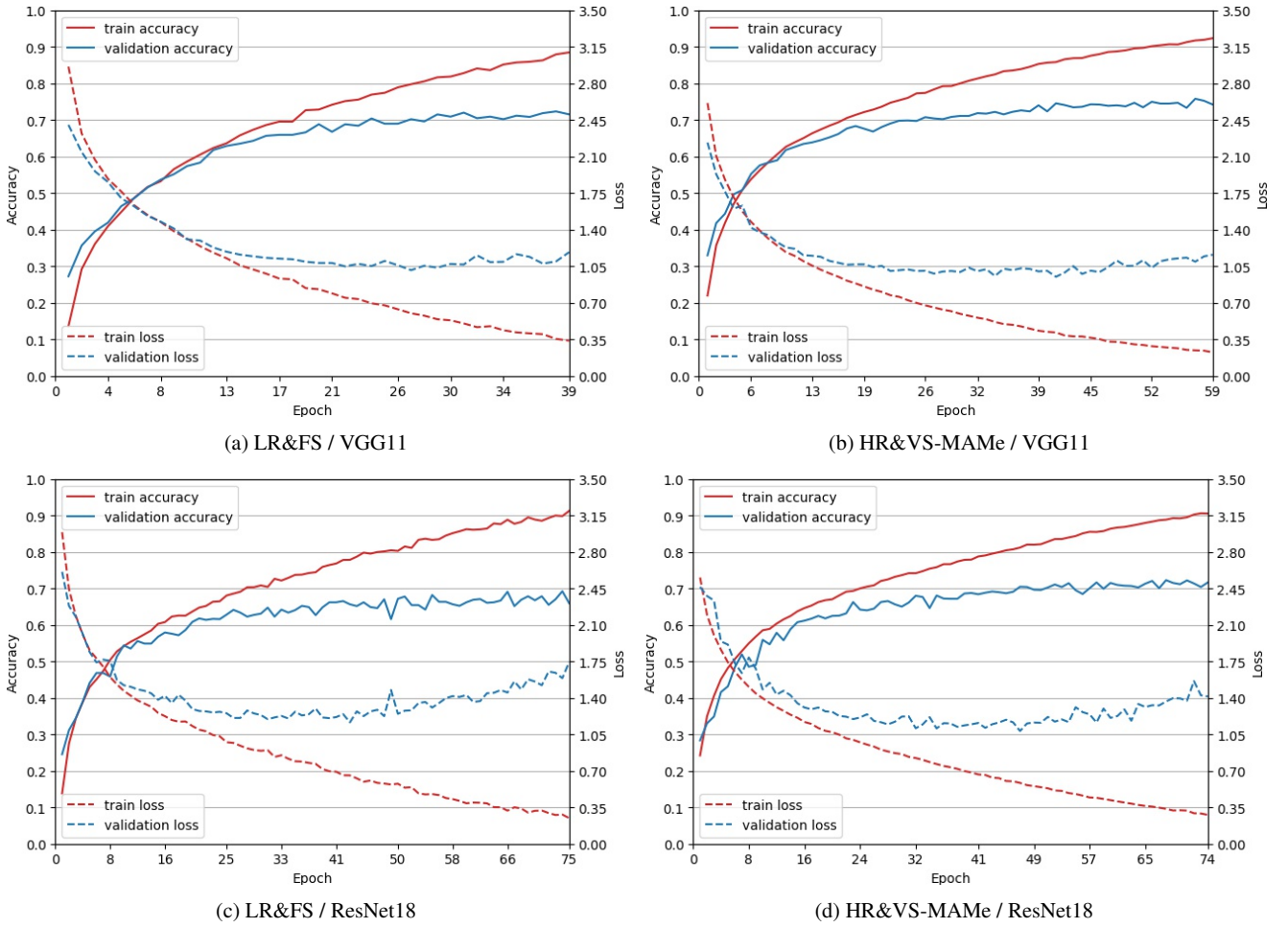


Fig. 5: Training curves for all baselines. Top row shows results for VGG11, bottom row for ResNet18. First column includes experiments using the low-resolution and fixed size input pipeline. Second column includes the high-resolution and variable shape pipeline.

5 Expert and Baseline Analysis of MAMe

The domain of artworks and heritage is defined by human technology, skill and creativity. Art experts can identify a set of visual queues useful for the characterization of art, but remains to be seen if AI models learn these same features. To analyze these features in the context of the MAMe dataset, we analyze several medium classes from an expert point of view and perform explainability experiments on the baselines introduced in the previous section. By understanding the focus of baselines, we can detect the most relevant class features according to these models. These explanations allow experts to assess the consistence of the decisions made, and detect the potential existence of bias in the baseline models, or even in the dataset. Additionally, to further explore the impact of working with HR data, we compare the explanations generated when trained with downsampled and deformed images and the alternative HR and aspect ratio

conserving version. For this analysis we focus on the results obtained by the VGG11 architecture, our best baseline.

5.1 Layer-wise relevance propagation

In our analysis we use post-hoc interpretability [28]: Methods used to interpret the model predictions once the model has been trained. For image classification, a widely used visual explanation are the saliency methods. These methods use saliency maps to show the features on the image that contribute to a prediction. In other words, which pixels in the input image are important for the classification task. Among this family of methods [38, 39, 41, 44, 52], we use Layer-wise Relevance Propagation (LRP) [25] which has been used in different fields performing meaningful explanations [6, 7, 43, 48]. The LRP technique backpropagates the output prediction to the input image, by computing the contribution of each neuron *w.r.t.* the output prediction. That is,

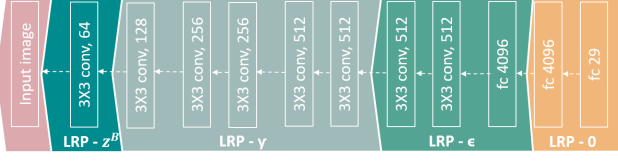


Fig. 6: LRP rules applied to each layer of the VGG11 network.

effectively mapping the relevance of an specific class into the pixels of the input image.

Although different LRP rules have been proposed, we implement the recent Composite LRP [31]. This technique proposes to combine different propagation rules depending on the depth of the layer. Our Composite LRP makes use of LRP-0 for last layers, LRP- ϵ ($\epsilon = 0.25$) and LRP- γ ($\gamma = 0.25$) for intermediate layers, and LRP- z^B for the first layer of the network, as illustrated in Figure 6.

So, given an image I and a specific class c , the Composite LRP produces an explanation heatmap $E_{I,c}$. The color convention for this heatmap is as follows: red is used for positive contributions, while blue indicates negative contributions. That means, the red areas are considered descriptive patterns of the given class by the model. Meanwhile, the blue areas are considered typical patterns of other classes.

We perform two types of LRP analysis, one for the correctly predicted images, and another one for the incorrectly predicted images. In case of correctly predicting the medium m , we produce its corresponding explanation heatmap $E_{I,m}$. In this case, the red areas of the heatmap correspond to descriptive patterns of the predicted medium m and blue areas to descriptive patterns of the rest of mediums. In the case of incorrectly predicted images, we computed the explanation as the difference between two heatmaps. The one associated to the real medium r , minus the one associated to the predicted medium p :

$$E_{I,r,p} = E_{I,r} - E_{I,p} \quad (1)$$

This difference allows to remove the contributions to the predicted class, focusing on the features that contribute to the real class. In this visualization, the red areas will be considered typical patterns of the real class but not of the predicted class, while blue areas will be considered typical patterns of other classes (most of them probably from the predicted class).

5.2 Best and worst performances

First, let us focus on the classes that are best and worst recognized by the baselines. That is, the ones with higher and lower mean F1-scores in Table 4. Among the best ones we can count *Albumen photograph*, *Gold* and *Graphite*. In the

case of *Albumen photograph*, we only have one type of photographic technique in the MAMe dataset, making these images easily distinguishable from other cultural assets. The class *Gold* is a similar case, since the golden color differentiates it from other metals, despite having other objects in the dataset of similar shapes. Lastly, *Graphite* is a drawing technique that uses similar grey tones with metallic brightness and smooth strokes that usually end at the edge of the paper. These characteristics help avoiding confusions between *Graphite* and *Lithograph*, which in some cases may be similar. For these reasons these mediums are easily recognizable, not only for the baseline models, but also for human experts.

On the other side of the spectrum we have the classes that are most poorly recognized according to Table 4. These include *Woven fabric*, *Polychromed wood*, *Etching* and *Silk and metal thread*. These classes are hard to predict because they belong to fine-grained groups of classes, with many common features. Following expert guidelines we identify the following fine-grained groups. These are discussed in further detail next.

- Prints: *Etching*, *Engraving*, *Wood engraving*, *Woodcut*, *Woodblock*, *Lithograph*
- Fabrics: *Woven fabric*, *Silk and metal thread*
- Paintings: *Polychromed Wood*, *Oil on canvas*

5.2.1 Prints group

From an expert perspective, the most complex fine-grained group is Prints. They are hard to differentiate because they may look very similar, despite having been printed through different procedures. Common clues used by experts for their discrimination include the definition of lines, the appearance of strokes, the homogeneity of shadows or color areas, as well as the intensity of blacks. A common feature used to identify different kinds of prints is the platemark. Platemark is the rectangular ridge created in the paper of a print by the edge of an intaglio plate. These marks can be essential for the discrimination of certain print classes: While both *Engraving* or *Wood engraving* have very defined lines and grid patterns, they can be told apart through platemarks since these only appear on the edges of an *Engraving*. Within the same group Prints, *Woodblocks* are distinguishable from the rest because of their oriental aesthetics. They are usually colored prints that use one block for each ink. As a result, colors sometimes overlap, and/or leave gaps in the outlines. However, this last characteristic is also found on other colored prints like *Lithographs* or *Woodcuts*. One last example to illustrate the complexity within Prints could be *Etching* and *Engraving*. These two techniques are very similar, having the same aforementioned platemarks and often the same grid patterns in their printed areas. In this case, experts need to appreciate the contours of the lines for differentiation. They are more



Fig. 7: Example of an *Engraving* artwork at its original size (left side) and HR&VS (right side). The second row shows the same zoomed area for both images, where the grid pattern can only be perceived on the original resolution (left). MET MUSEUM: 53.600.1616

vibrant and less defined in *Etchings*, and they have convex edges for *Engravings*.

In sight of the expert knowledge, image resolution seems key to properly detect main discriminating patterns. In some cases, even our HR&VS images seem to fall short in resolution (e.g., grid patterns are lost). As an example, Figure 7 shows a rectangular region of an *Engraving* in original resolution (left side) and in HR&VS (right side). Zoomed area shows the central figure of the print, a fisherman. If we focus on the clothes, we can clearly perceive the characteristic grid pattern of an *Engraving* in the original resolution image, but these are lost on the HR&VS image, where the grid become a gray blur due to the interpolation when resizing the image.

5.2.2 Fabrics group

The second group of fine-grained classes is *Fabrics*. To discriminate these with total confidence it is necessary to identify the fibers using microscopy techniques. This condition motivated the aggregation of several classes within *Woven fabric* (e.g., linen, cotton, silk and others). Nonetheless, one particular type of woven fabric can be visually recognized without the aid of external machinery. That is *Silk and metal thread*, which are clearly distinguishable from other textile fibers due to the glitter of metallic threads.

In Figure 8, we can see the metallic glitter in both images LR&FS and HR&VS (more clearly on the latter). However, the baseline models have been unable to properly discriminate these two classes. If the model does not detect this feature, it will learn other patterns for differentiating these two classes, such as ornamental motifs. However, this is not

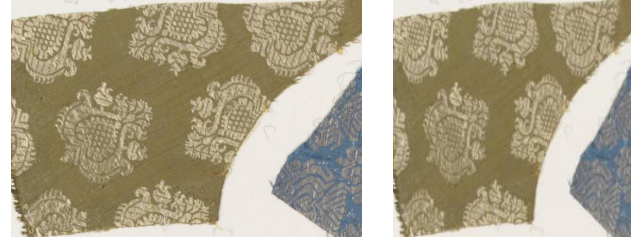


Fig. 8: Example of *Silk and metal thread* in HR&VS (left) and LR&FS (right). The brightness of the metal threads is visible in both cases.

MET MUSEUM: 2002.494.278



Fig. 9: Example of *Silk and metal thread* in HR&VS (left) and its LRP explanation (right). The ornamental motifs (red zones) have positively contributed to the *Silk and metal thread* class classification.

MET MUSEUM: 2002.494.366

a reliable discriminatory feature and, therefore, it could be a source of error. We performed explainability experiments on several images and found cases where the model focuses on the ornamental motifs as shown in Figure 9.

5.2.3 Paintings group

The third group of fine-grained classes is *Paintings*. This group contains two classes: *Polychromed wood* and *Oil on canvas*. The main reason why these classes are hard to differentiate is because *Polychromed wood* contains the sub-class panel paintings (i.e., a painting on a flat panel made of wood), which are similar to *Oil on canvas*. Both, *Polychromed wood* panel paintings and *Oil on canvas*, hide the support behind the paint layer, complicating the identification of the support material (fabric or wood). In this context, experts pay attention to cracks, leaks or textures that may be characteristic of the support below the paint. Nonetheless, these features may not be properly visible in a single LR&FS or HR&VS images.

There are several *Oil on canvas* images that are incorrectly predicted as *Polychromed wood*, both in LR&FS and

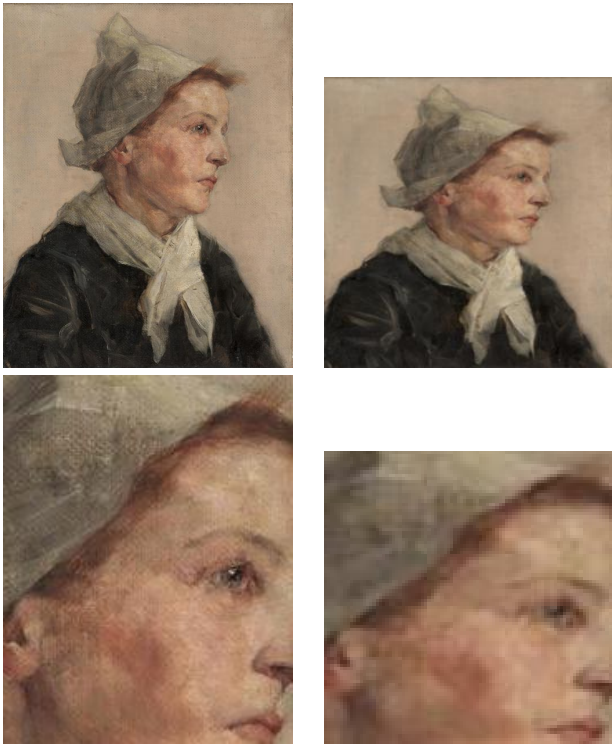


Fig. 10: Example of *Oil on canvas* in HR&VS (left side) and LR&FS (right side). The second row shows the zoomed area where it is possible to perceive the canvas wave pattern in the HR&VS but not in the LR&FS image.
CLEVELAND MUSEUM: 1943.324

in HR&VS. It makes sense from an expert point of view since, in several HR&VS images, it is impossible to appreciate any detail that may suggest whether the support is wood or fabric, forcing the model to guess the class based on alternative patterns that may be misleading. For example, one of the key properties that identify an *Oil on canvas* is the canvas weave pattern. Unfortunately, this seems to be visible only on a few HR&VS images. Within this work, art experts reviewed around 150 images where the models failed to discriminate between *Oil on canvas* and *Polychromed wood*, and considered that they could only see the canvas weave pattern in approximately 5% of the HR&VS images. In Figure 10, we show an example of an *Oil on canvas* image where it is possible to perceive the canvas weave pattern. Although this pattern is present in the HR&VS image but not in the LR&FS image, both models misclassified this example, indicating that the HR&VS model does not pay attention to this property.

5.3 LR&FS and HR&VS comparison

In this section we explore the classes with greatest difference in accuracy between baselines (as shown in Table 4). In order, these are *Lithograph* (+16.28% gain by

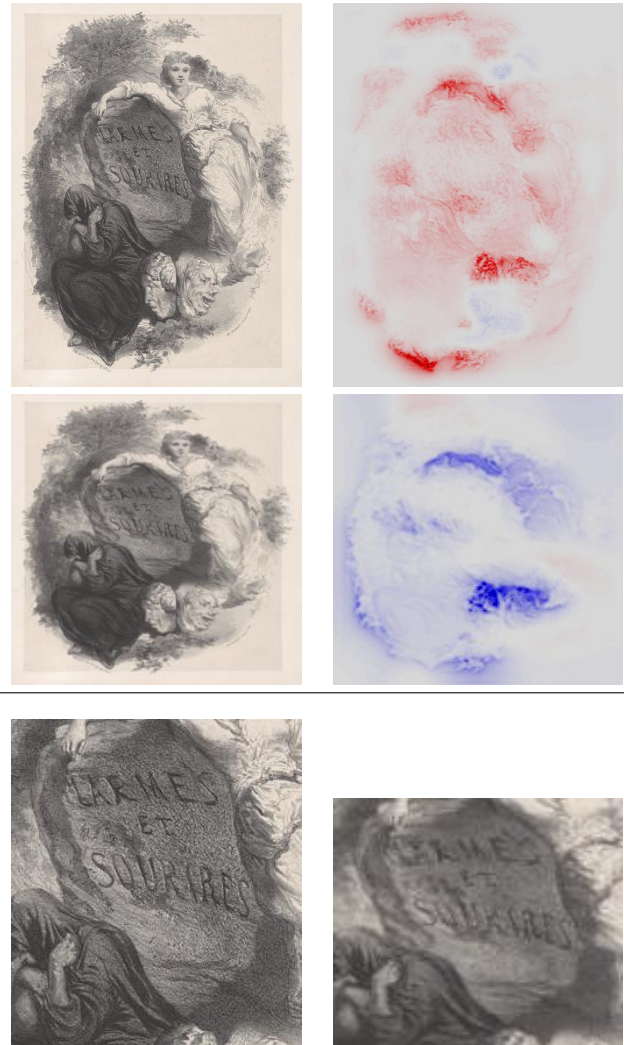


Fig. 11: *Lithograph* example in HR&VS and LR&FS. There is a top side and a bottom side divided by a horizontal black line. Top shows the image in HR&VS and its corresponding LRP explanation. Both models focus on the general texture for their predictions, although LR&FS mispredicts *Wood engraving*. Bottom side shows a zoomed area of the print in HR&VS (left) and LR&FS (right). In here we can see the granular texture of the surface typical of this class in HR&VS, but not in LR&FS.

MET MUSEUM: 49.21.53

HR&VS), *Bronze* (+15.71% gain by HR&VS) and *Engraving* (+14.85% gain by HR&VS). *Lithograph* and *Engraving* are within the *Prints* group which, as reviewed in §5.2.1, can benefit from more detailed inputs for their discrimination. The third, *Bronze* is a material which can be easily differentiated by a human expert.

Let us start with the case of *Lithograph*. Figure 11 shows a representative example of this class, illustrating both the input and the LRP for the HR&VS and LR&FS models. Both models focus on the overall texture of the image (the LRP relevance is spread throughout the image), but with dif-



Fig. 12: *Engraving* example in HR&VS and LR&FS and its corresponding LRP explanations. Check how the contours of the figures positively contribute to the prediction of the class in HR&VS format. LR&FS loses most these details, and mispredicts it as *Wood engraving*.
CLEVELAND MUSEUM: 1958.105

ferent impacts on the prediction: it represents negative evidence for LR&FS (which ends up in mispredicting the class *Wood engraving*) but positive evidence for HR&VS. Experts highlight the relevance of the texture of *Lithographs* for their discrimination from other similar classes like *Woodblock*, *Hand-colored etching*, *Wood engraving* or *Hand-colored engraving*. *Lithographs* contain a granular texture that is not present on the other classes, but this texture is only visible at a certain resolution, as shown in the zoomed tombstone at the bottom of Figure 11. This LRP results indicate that the HR&VS baseline model follows a similar strategy to distinguish *Lithograph* from other classes, successfully recognizing the textures from prints and properly interpreting them for the final prediction. The LR&FS model, unable to recognize the granular texture, fails at finding relevant features towards *Lithograph*.

Figure 12 shows an example of the *Engraving* class, which has been correctly predicted by the HR&VS but not by the LR&FS (mispredicted as *Wood engraving*). The Figure contains the entire image and its corresponding LRP explanation for both, HR&VS and LR&FS, which target really different aspects of the print: While HR&VS focuses on the contours of the print figures, LR&FS does not. According to experts, these figure contours are dark areas that encode essential information for discriminating

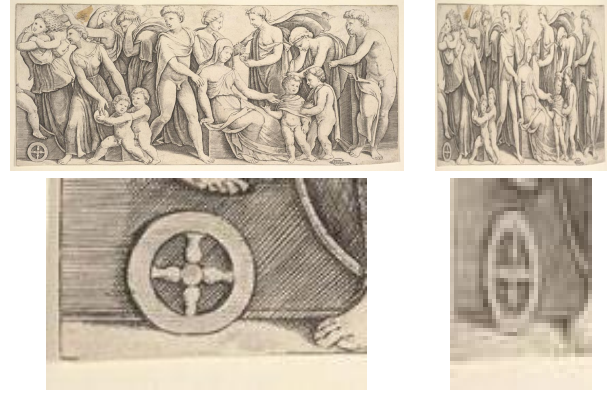


Fig. 13: First row shows an *Engraving* in HR&VS and LR&FS. Notice the deformation of the latter. Second row shows a zoomed area, to illustrate how the grid lines become blurred in the LR&FS version.
MET MUSEUM: 17.3.3169

the mediums within the *Prints* group. Contours can only be properly inspected at high-resolutions. Some of this information is retained in HR&VS images, as reviewed by experts. Meanwhile LR&FS images lose all relevant details.

As mentioned in subsection 5.2.1, another property to distinguish printing techniques is the grid pattern. Although in some cases it can only be perceived in the original resolution image, some HR&VS image retain this information. However, this is always lost in the LR&FS images. On top of that, the image distortion produced by the shape variation of LR&FS images forces the grid lines closer in one axis (unpredictably, as it depends on the original image aspect ratio), complicating its identification. As an example of that, Figure 13 shows an *Engraving* image in HR&VS and LR&FS format, where the latter shows a great image distortion. It also shows a zoomed area, highlighting the differences in the grid pattern.

The last case we consider in this section is the third class with the biggest difference in performance. This is the *Bronze* class, which includes a great variety of objects (e.g., sculptures, ornaments), but specially coins. One of the main reasons why there are so many coins inside the *Bronze* class is that, historically, *Bronze* has been a usual alloy used to mint coins. One of the main characteristics of a coin is its circular shape. However, this property is lost when deforming the image due to the uniformization of aspect ratio inherent to LR&FS inputs. The lack of a uniform shape of coins has a negative impact on their recognition, which is not found on the HR&VS baseline models. A clear example of this can be observed in Figure 14. The corresponding LRP explanations show, on one side, the positive impact of the rounded coin contour for the HR&VS image and, on the other side, the negative impact of the deformed coin for the prediction of the LR&FS image. This particular LR&FS example is

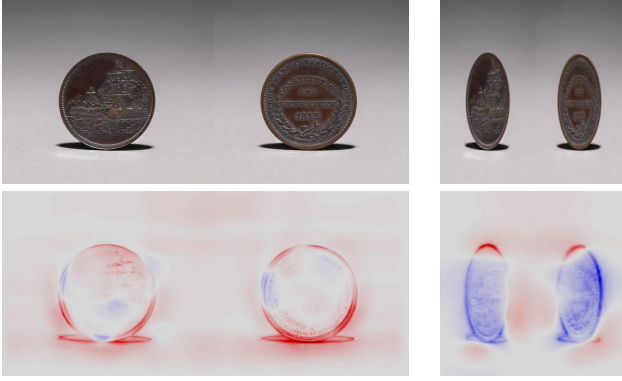


Fig. 14: Example of coins within the *Bronze* class in HR&VS (left side) and LR&FS (right side), and its corresponding LRP explanations (bottom). Shape of coins is lost in LR&FS, which affects the prediction.
CLEVELAND MUSEUM: 1916.1877



Fig. 15: Zoom in of a *Bronze* artwork in HR&VS (left) and in LR&FS (right) respectively. Notice how the corrosion and patinas are easier to appreciate in HR&VS.
CLEVELAND MUSEUM: 1926.248

mispredicted with *Steel*, which makes sense from an expert point of view because the model must focus on the detection of the material, as it can not rely on the shape of the coin for the prediction. Indeed, classes like *Steel* and *Iron* are among the most frequent confusions for *Bronze*. As a result, *Bronze* is significantly better predicted by the HR&VS, with a 15.7% increase in accuracy with respect to LR&FS.

Another example is shown in Figure 15, where we can see the characteristic corrosion and patinas of *Bronze*. This corrosion or green patinas on the surface comes from the oxidation of copper, which is one of the main components of the *Bronze* alloy. Experts underline that these properties make quite easy to recognize the class. While these are perfectly visible in HR&VS images, they become hard to perceive in the LR&FS images.

6 Conclusions

In this paper, we introduce the MAMe dataset, a novel challenge for the prediction of artwork mediums based on its

visual appearance. The images of the dataset come from three different museums for a total of 37,407 images. Museums do not share a common scheme for labeling mediums, which required intensive work by art experts for its homogenization. For producing the dataset, we leverage technical requirements (sample size, balance, image resolution, *etc.*) and domain requirements (visual coherency, taxonomical properties, *etc.*). At the end, the MAMe is composed by 29 classes of mediums, each containing at least 850 images (always 700 for training) of high-resolution (at least 500 pixels in the smaller axis) and variable shape.

In comparison with commonly available datasets, the MAMe provides a significantly larger distribution of high-resolution and variable-shaped images. These properties are of relevance in future applications of image processing for domains such as medicine or autonomous driving. Visual challenges where attention to detail, understanding the overall structure of the image and avoiding information deformation/loss is crucial. Recognizing a lack of focus on these topics by the AI community, MAMe provides a good testing ground for new research ideas in the field.

Baseline results (see Figure 3 and 5) show two main conclusions. First, that interpolating images to a small size and squared shape has a negative impact on the performance. Further experimentation with more architectures is required to generalize this conclusion. An ablation study is also needed to assess the impact of each factor (*i.e.*, high-resolution and variable shape) separately. Second, the baseline models are capable of solving the task proposed by the MAMe dataset up to a certain degree. This provides empirical evidence that, on one hand, the MAMe dataset proposes a solvable task and, on the other hand, there is room for improvement on its resolution. We hope that these results motivate the community to tackle this task, trying to improve the baseline results through novel methods or architectures that benefit from high-resolution and variable-shaped properties.

To further understand the behavior of the trained baselines, we perform explainability experiments using the LRP method. These allow us to assess how the baseline models fail to discriminate between certain classes due to a lack of resolution. In several cases we found that the HR&VS resolution is insufficient to perceive the patterns that experts would pay attention to. This forces the models to learn on alternative patterns that may not generalize well. Further increasing the resolution was impossible due to memory requirement limitations, which points to another future line of research. Both for the computer architecture community (designing hardware with larger capacities) and the AI community (designing more memory efficient methods).

Acknowledgements This work is partially supported by the Intel-BSC Exascale Lab agreement, by the Spanish Government through

Programa Severo Ochoa (SEV-2015-0493), by the Spanish Ministry of Science and Technology through TIN2015-65316-P project, by the Generalitat de Catalunya (contracts 2017-SGR-1414) and by the Secretaria d'Universitats i Recerca of the Generalitat de Catalunya under the Industrial Doctorate Grant DI 2018-100. Authors would like to thank the support and assessment of the Conservaci- Restauraci del Patrimoni group (2017-SGR-1151).

References

1. Beyond imagenet large scale visual recognition challenge. http://image-net.org/challenges/beyond_ilsvrc. Accessed: 2019-11-14
2. Cleveland museum: Open access. <https://www.clevelandart.org/open-access>. Accessed: April 2020
3. Lacma launches new collections online website. <https://www.lacma.org/press/lacma-launches-new-collections-online-website>. Accessed: April 2020
4. Met museum: Image and data resources. <https://www.metmuseum.org/about-the-met/policies-and-documents/image-resources>. Accessed: April 2020
5. Printmaking descriptions. <https://www.metmuseum.org/about-the-met/curatorial-departments/drawings-and-prints/materials-and-techniques/printmaking>. Accessed: May 2020
6. Arbabzadah, F., Montavon, G., Müller, K.R., Samek, W.: Identifying individual facial expressions by deconstructing a neural network. In: B. Rosenhahn, B. Andres (eds.) *Pattern Recognition*, pp. 344–354. Springer International Publishing, Cham (2016)
7. Binder, A., Bockmayr, M., Hgele, M., Wienert, S., Heim, D., Hellweg, K., Stenzinger, A., Parlow, L., Budczies, J., Goepfert, B., Treue, D., Kotani, M., Ishii, M., Dietel, M., Hocke, A., Denkert, C., Mller, K.R., Klauschen, F.: Towards computational fluorescence microscopy: Machine learning-based integrated prediction of morphological and molecular tumor profiles (2018)
8. Bossard, L., Guillaumin, M., Van Gool, L.: Food-101—mining discriminative components with random forests. In: *European Conference on Computer Vision*, pp. 446–461. Springer (2014)
9. Chen, X., Ma, H., Wan, J., Li, B., Xia, T.: Multi-view 3d object detection network for autonomous driving. In: *Proceedings of the IEEE Conference on Computer Vision and Pattern Recognition*, pp. 1907–1915 (2017)
10. Cimpoi, M., Maji, S., Kokkinos, I., Mohamed, S., Vedaldi, A.: Describing textures in the wild. In: *Proceedings of the IEEE Conference on Computer Vision and Pattern Recognition*, pp. 3606–3613 (2014)
11. Everingham, M., Van Gool, L., Williams, C.K.I., Winn, J., Zisserman, A.: The PASCAL Visual Object Classes Challenge 2012 (VOC2012) Results. <http://www.pascal-network.org/challenges/VOC/voc2012/workshop/index.html>
12. Foundation, C.V.D.: Google landmarks v2 dataset. <https://github.com/cvdfoundation/google-landmark#release-history> (2019)
13. Geras, K.J., Wolfson, S., Shen, Y., Wu, N., Kim, S., Kim, E., Heacock, L., Parikh, U., Moy, L., Cho, K.: High-resolution breast cancer screening with multi-view deep convolutional neural networks. *arXiv preprint arXiv:1703.07047* (2017)
14. Ghosh, S., Das, N., Nasipuri, M.: Reshaping inputs for convolutional neural network: Some common and uncommon methods. *Pattern Recognition* **93**, 79–94 (2019)
15. Glorot, X., Bengio, Y.: Understanding the difficulty of training deep feedforward neural networks. In: *Proceedings of the thirteenth international conference on artificial intelligence and statistics*, pp. 249–256 (2010)
16. Griffin, G., Holub, A., Perona, P.: Caltech-256 object category dataset (2007)
17. He, K., Gkioxari, G., Dollár, P., Girshick, R.: Mask r-cnn. In: *Proceedings of the IEEE international conference on computer vision*, pp. 2961–2969 (2017)
18. He, K., Zhang, X., Ren, S., Sun, J.: Delving deep into rectifiers: Surpassing human-level performance on imagenet classification. In: *Proceedings of the IEEE international conference on computer vision*, pp. 1026–1034 (2015)
19. He, K., Zhang, X., Ren, S., Sun, J.: Spatial pyramid pooling in deep convolutional networks for visual recognition. *IEEE transactions on pattern analysis and machine intelligence* **37**(9), 1904–1916 (2015)
20. He, K., Zhang, X., Ren, S., Sun, J.: Deep residual learning for image recognition. In: *Proceedings of the IEEE conference on computer vision and pattern recognition*, pp. 770–778 (2016)
21. Huang, Y., Cheng, Y., Bapna, A., Firat, O., Chen, D., Chen, M., Lee, H., Ngiam, J., Le, Q.V., Wu, Y., et al.: Gpipe: Efficient training of giant neural networks using pipeline parallelism. In: *Advances in Neural Information Processing Systems*, pp. 103–112 (2019)
22. Khosla, A., Jayadevaprakash, N., Yao, B., Li, F.F.: Novel dataset for fine-grained image categorization: Stanford dogs. In: *Proc. CVPR Workshop on Fine-Grained Visual Categorization (FGVC)*, vol. 2 (2011)
23. Kingma, D.P., Ba, J.: Adam: A method for stochastic optimization. *arXiv preprint arXiv:1412.6980* (2014)
24. Kuznetsova, A., Rom, H., Alldrin, N., Uijlings, J., Krasin, I., Pont-Tuset, J., Kamali, S., Popov, S., Mallocci, M., Duerig, T., Ferrari, V.: The open images dataset v4: Unified image classification, object detection, and visual relationship detection at scale. *arXiv:1811.00982* (2018)
25. Lapuschkin, S., Binder, A., Montavon, G., Klauschen, F., Mller, K.R., Samek, W.: On pixel-wise explanations for non-linear classifier decisions by layer-wise relevance propagation. *PLoS ONE* **10**, e0130140 (2015). DOI 10.1371/journal.pone.0130140
26. Lin, T.Y., Dollár, P., Girshick, R., He, K., Hariharan, B., Belongie, S.: Feature pyramid networks for object detection. In: *Proceedings of the IEEE conference on computer vision and pattern recognition*, pp. 2117–2125 (2017)
27. Lin, T.Y., Maire, M., Belongie, S., Hays, J., Perona, P., Ramanan, D., Dollár, P., Zitnick, C.L.: Microsoft coco: Common objects in context. In: *European conference on computer vision*, pp. 740–755. Springer (2014)
28. Lipton, Z.: The mythos of model interpretability: In machine learning, the concept of interpretability is both important and slippery. *Queue* **16** (2018)
29. Lotter, W., Sorensen, G., Cox, D.: A multi-scale cnn and curriculum learning strategy for mammogram classification. In: *Deep Learning in Medical Image Analysis and Multimodal Learning for Clinical Decision Support*, pp. 169–177. Springer (2017)
30. Maynor, C.I., Reyden, D.: Paper conservation catalog. The American Institute for Conservation of Historic and Artistic Works Book and Paper Group. Ninth Edition. (1993)
31. Montavon, G., Binder, A., Lapuschkin, S., Samek, W., Mller, K.R.: Layer-Wise Relevance Propagation: An Overview, pp. 193–209 (2019). DOI 10.1007/978-3-030-28954-6_10
32. Nair, V., Hinton, G.E.: Rectified linear units improve restricted boltzmann machines. In: *Proceedings of the 27th international conference on machine learning (ICML-10)*, pp. 807–814 (2010)
33. Nilsback, M.E., Zisserman, A.: Automated flower classification over a large number of classes. In: *Computer Vision, Graphics & Image Processing, 2008. ICVGIP'08. Sixth Indian Conference on*, pp. 722–729. IEEE (2008)

34. Parkhi, O.M., Vedaldi, A., Zisserman, A., Jawahar, C.: Cats and dogs. In: Computer Vision and Pattern Recognition (CVPR), 2012 IEEE Conference on, pp. 3498–3505. IEEE (2012)
35. Quattoni, A., Torralba, A.: Recognizing indoor scenes. In: Computer Vision and Pattern Recognition, 2009. CVPR 2009. IEEE Conference on, pp. 413–420. IEEE (2009)
36. Reddi, S.J., Kale, S., Kumar, S.: On the convergence of adam and beyond. arXiv preprint arXiv:1904.09237 (2019)
37. Russakovsky, O., Deng, J., Su, H., Krause, J., Satheesh, S., Ma, S., Huang, Z., Karpathy, A., Khosla, A., Bernstein, M., et al.: Imagenet large scale visual recognition challenge. *International journal of computer vision* **115**(3), 211–252 (2015)
38. Selvaraju, R.R., Cogswell, M., Das, A., Vedantam, R., Parikh, D., Batra, D.: Grad-cam: Visual explanations from deep networks via gradient-based localization. *International Journal of Computer Vision* **128**(2), 336359 (2019). DOI 10.1007/s11263-019-01228-7. URL <http://dx.doi.org/10.1007/s11263-019-01228-7>
39. Simonyan, K., Vedaldi, A., Zisserman, A.: Deep inside convolutional networks: Visualising image classification models and saliency maps (2013)
40. Simonyan, K., Zisserman, A.: Very deep convolutional networks for large-scale image recognition. arXiv preprint arXiv:1409.1556 (2014)
41. Springenberg, J.T., Dosovitskiy, A., Brox, T., Riedmiller, M.: Striving for simplicity: The all convolutional net (2014)
42. Srivastava, N., Hinton, G., Krizhevsky, A., Sutskever, I., Salakhutdinov, R.: Dropout: a simple way to prevent neural networks from overfitting. *The journal of machine learning research* **15**(1), 1929–1958 (2014)
43. Sturm, I., Bach, S., Samek, W., Müller, K.: Interpretable deep neural networks for single-trial EEG classification. *CoRR abs/1604.08201* (2016). URL <http://arxiv.org/abs/1604.08201>
44. Sundararajan, M., Taly, A., Yan, Q.: Axiomatic attribution for deep networks (2017)
45. Szegedy, C., Liu, W., Jia, Y., Sermanet, P., Reed, S., Anguelov, D., Erhan, D., Vanhoucke, V., Rabinovich, A.: Going deeper with convolutions. In: Proceedings of the IEEE conference on computer vision and pattern recognition, pp. 1–9 (2015)
46. Szegedy, C., Vanhoucke, V., Ioffe, S., Shlens, J., Wojna, Z.: Rethinking the inception architecture for computer vision. In: Proceedings of the IEEE conference on computer vision and pattern recognition, pp. 2818–2826 (2016)
47. Tan, M., Le, Q.V.: Efficientnet: Rethinking model scaling for convolutional neural networks. arXiv preprint arXiv:1905.11946 (2019)
48. Thomas, A.W., Heekeren, H.R., Müller, K.R., Samek, W.: Interpretable lstms for whole-brain neuroimaging analyses. Preprint at <https://arxiv.org/abs/1810.09945> (2018)
49. Trembl, M., Arjona-Medina, J., Unterthiner, T., Durgesh, R., Friedmann, F., Schuberth, P., Mayr, A., Heusel, M., Hofmarcher, M., Widrich, M., et al.: Speeding up semantic segmentation for autonomous driving. In: MLITS, NIPS Workshop, vol. 2, p. 7 (2016)
50. Wu, X., Zhan, C., Lai, Y.K., Cheng, M.M., Yang, J.: Ip102: A large-scale benchmark dataset for insect pest recognition. In: Proceedings of the IEEE Conference on Computer Vision and Pattern Recognition, pp. 8787–8796 (2019)
51. Xie, Q., Hovy, E., Luong, M.T., Le, Q.V.: Self-training with noisy student improves imagenet classification (2019)
52. Zeiler, M.D., Fergus, R.: Visualizing and understanding convolutional networks (2013)
53. Zhou, B., Lapedriza, A., Khosla, A., Oliva, A., Torralba, A.: Places: A 10 million image database for scene recognition. *IEEE transactions on pattern analysis and machine intelligence* **40**(6), 1452–1464 (2017)
54. Zoph, B., Vasudevan, V., Shlens, J., Le, Q.V.: Learning transferable architectures for scalable image recognition. In: Proceedings of the IEEE conference on computer vision and pattern recognition, pp. 8697–8710 (2018)